Parameter optimization for a scraping-rotating-brushing dehilling machine using EDEM

Shuming Yang[1], Zheng Cui[1], Qian Wang[2], Dehua Gao[1], Maoqiang Li[3], Yutan Wang[1], Jinhai Li[1*]
(1. *Ningxia University, Yinchuan 750021, Ningxia, China*;
2. *Ningxia Academy of Agriculture and Forestry Sciences, Yinchuan 750021, Ningxia, China*;
3. *North Minzu University, Yinchuan 750021, Ningxia, China*)

Abstract: The eastern foot of Helan Mountain in the Ningxia Hui Autonomous Region stands out as one of the prime grape-growing regions in China. Owing to the dry, cold, and windy winter climate of the region, it is common practice to cover grapevines with soil and form ridges for winter protection. These soil ridges are cleared in the subsequent spring to allow grapevines to grow unhindered. However, conventional dehilling machines often demonstrate a low soil-clearing rate, leaving a significant amount of residual soil behind. This inefficiency necessitates labor-intensive manual soil removal processes. To address this challenge, a scraping-rotating-brushing dehilling machine was designed. The discrete element method (DEM) was utilized to determine the optimal structural parameters for the critical components, including the scraper, rotary blade, and flexible brush. DEM models were constructed for the scraper alone, the scraper-rotary blade combination, and the scraper-rotary blade-brush combination to simulate their respective working processes. Through simulation analysis, the optimal combination parameters of the physical prototype were obtained. Field experiments were conducted to measure the clearing rate of the scraping-rotating-brushing dehilling machine, revealing an extremely low relative error of just 0.05% between the DEM simulation results and the field test outcomes. This confirms the accuracy of our DEM model. The success of the DEM model implementation highlights its potential in the design and development of grape soil-clearing machinery. This innovative approach not only reduces the cost associated with prototype development but also provides reference for the research and development of other related agricultural machinery.

Keywords: DEM, grape, soil removal operation, simulation, parameter optimization
DOI: 10.25165/j.ijabe.20241706.8821

Citation: Yang S M, Cui Z, Wang Q, Gao D H, Li M Q, Wang Y T, et al. Parameter optimization for a scraping-rotating-brushing dehilling machine using EDEM. Int J Agric & Biol Eng, 2024; 17(6): 142–155.

1 Introduction

The eastern foothills of Helan Mountain in Ningxia Hui Autonomous Region of China provide an excellent environment for grape cultivation, thanks to the region's favorable soil and water conditions[1,2]. Wine grapes require specific environmental conditions, with the optimal average growth temperature needing to be above 15°C[3,4]. The significant diurnal temperature variations in northern China enhance the fruit's sugar accumulation, yet grapevines in this region are also prone to frost damage due to the extremely low winter temperatures[5-7]. Consequently, this region needs to implement measures to ensure the safe overwintering of grapevines[8]. This involves burying the grapevines under a frame to form a soil ridge before winter. The soil ridge is then removed, and the grapevines are secured to the frame after the temperature rises. Clearing vineyard soil ridges is a seasonal activity that is closely monitored[9-11]. Currently, the primary method involves a combination of mechanical and manual labor for segmented soil clearing, resulting in low efficiency, high labor intensity, and increased operational costs. To facilitate the intelligent development of the grape industry, the advancement of soil-clearing machinery is an inevitable and crucial trend.

The European region benefits from a mild climate for viticulture, which results in a lower risk of grapevines suffering from freezing and wind-drying. This is primarily achieved through the careful selection of suitable grape varieties and winter pruning to adjust the grapevines' relationship with their environment, ensuring safe overwintering[12,13]. The cold climate in North America makes viticulture even riskier. Therefore, ensuring the safe overwintering of grapes involves both active and passive approaches, with a focus on selecting cold-resistant grape varieties and rootstocks, as well as using appropriate scion-rootstock combinations. Additionally, heaters, insulation, and snow coverings are employed to minimize heat loss from the vines[14,15]. Consequently, research on soil-clearing machinery has been limited in this region.

In contrast, the Asian region has experienced rapid advancements in soil-clearing machinery in recent years. Contact-based soil-clearing machines, which are widely used, provide high efficiency. However, they tend to increase overall power consumption, intensify cutter vibrations, and accelerate cutter

---

Received date: 2024-01-18 **Accepted date:** 2024-10-21

Biographies: Shuming Yang, PhD, research interest: smart agricultural equipment, Email: shmyang@nxu.edu.cn; **Zheng Cui**, MS, research interest: smart agricultural equipment, Email: CZwow0218@163.com; **Qian Wang**, MS, research interest: smart agricultural equipment, Email: wangqian951229@163.com; **Dehua Gao**, PhD, research interest: smart agricultural equipment, Email: dehuag@nxu.edu.cn; **Maoqiang Li**, PhD, research interest: smart agricultural equipment, Email: li-maoqiang408412@163.com; **Yutan Wang**, PhD, research interest: image processing and deep learning, Email: wang_yt@nxu.edu.cn.

***Corresponding author: Jinhai Li**, PhD, research interest: agricultural information perception and smart agricultural equipment. No.489, Helanshan West Road, Xixia District, Yinchuan 750021, China. Tel: +86-18295695017, Email: lijinhai@nxu.edu.cn.

wear[16,17]. The components of soil-clearing machinery that come into direct contact with the soil significantly affect the efficiency of soil-clearing operations, and their structural parameters are critically important[18,19]. To enhance operational efficiency, scholars have investigated the application of the discrete element method (DEM) to optimize the parameters of soil-clearing tools through simulation experiments. Consequently, numerous scholars have conducted extensive research on the interaction between the working parts and the soil[20-22].

Xiong et al.[19] developed a simulation model that focuses on the interaction between the scraper and the soil using the discrete element particle contact theory. They validated the relationship between torque and rotational speed, providing valuable insights for analyzing energy consumption in scraper operations. Ma et al.[23] utilized the hysteretic spring contact model (HSCM) and the linear cohesion model (LCM) as the contact models for soil particles. They conducted a comprehensive rotational center combination simulation experiment using EDEM to determine the optimal parameters for soil contact. Zhao et al.[24] established a bionic digging shovel model with 37 roots and planting soil as the research object, analyzed the soil-bonding mechanism, and conducted soil groove experiments to improve the drag reduction rate of the bionic digging shovel to 24.29%. Qing et al.[25] established a simulation model of machinery, straw, and soil based on discrete element simulation and verified the cultivator's and the driven disk plow's straw-burying performance and soil layer exchange performance, respectively. Ahmad et al.[26] used discrete elements to model the pan groove opener in paddy soil and determined the optimal parameters under different working conditions through simulation experiments. Katinas et al.[27] used the discrete element method to simulate the influence of motion resistance on the operating parts of the bulldozer. They explored the influence of the type of sand on the wear of the working parts during the operation, laying a foundation for the parameter optimization of the parts. Zhang et al.[28] extracted the contour information of the mole toe based on the bionic principle, established the optimization model of the inner and outer contour fitting function by using the discrete element method, and obtained the optimal fitting function of the outer contour point cloud, which laid the foundation for the design of the disc plow in the high-viscosity soil environment. Kim et al.[29] carried out plowing experiments through the field load measurement system, established a full-size soil-tool coupling model based on DEM and MBD, predicted tractive force according to tillage depth, and reflected the distribution of soil properties with depth. The tractive force prediction accuracy reached 90.8%. Generally, the Ningxia region of China features high altitudes, complex vineyard terrain, and hard soils. Existing soil-clearing machines were not well-suited for soil clearing in this region. However, using DEM to simulate the mechanical structure and operational dynamics of agricultural machinery can significantly enhance their performance and efficiency[30-32]. Therefore, it was crucial to employ DEM to optimize the structural parameters of soil-clearing machinery, enabling it to meet the demands of spring soil clearing for wine grape cultivation in the Ningxia region.

In summary, this paper proposed an optimization method for soil-clearing machinery, focusing on the scraping-rotating-brushing type dehilling machine used in the Ningxia region. This method utilized a DEM model to simulate the interaction between the machine's working components and the soil. The study involved designing a single-factor test, a second-order central composite design, and an orthogonal test to determine the optimal parameter combination. Finally, the optimized parameters were validated through field tests to ensure their accuracy.

2 Materials and methods

2.1 Structure of scraping-rotating-brushing dehilling machine

2.1.1 Overall structure

The overall structure of the scraping-rotating-brushing dehilling machine consisted of a frame, a scraper, a rotary blade, a flexible brush, and the hydraulic device, all of which are depicted in Figure 1. The frame consisted of a suspension frame, a tie rod, a main frame, and a sub-frame. The bottom of the suspension frame was fixed to the main frame with a pin connection, while the top was connected to the tie rod by a pin. The sub-frame was placed inside the hollow square tube of the main frame, and the tie rod was connected to both the suspension frame and the main frame via pins. The scraper section, rotary blade section, and flexible brush section will be described individually in the following sections. In the operation process, under the joint action of tractor traction and hydraulic device, the scraper, rotary blade, and flexible brush successively cleared the soil on the side of the soil ridge, the bottom of the soil ridge, and the vine, completing the grape soil-clearing operation. The main technical parameters of the machine are shown in Table 1.

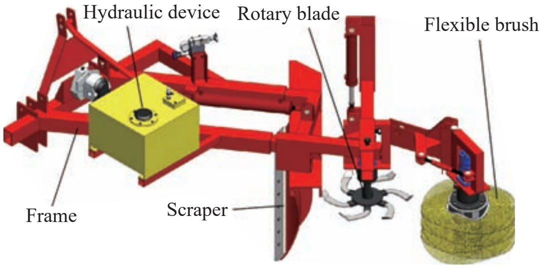

Figure 1 Overall structure of scraping-rotating-brushing dehilling machine

Table 1 The main technical parameters

Item	Technical parameters
Overall dimensions/mm	3000×2300×1500
Matching power/hp	120
Working width/mm	2 100
Operation speed/m·s^{-1}	0.8

2.1.2 Structure of the scraper

The prototype scraper consists of several key components, including a beam, an earth-contact surface, and a blade, as illustrated in Figure 2. In the process of scraper operation, under the action of tractor traction, the forward speed v_m makes a uniform linear motion to scrape the soil on the side of the ridge to the vineyard passage.

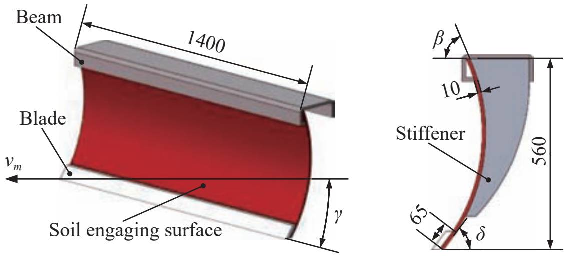

a. Axonometric drawing b. Side view

Figure 2 Structural diagram of the scraper

The scraper surface was designed to move horizontally along an arc, thereby performing functions such as pushing, moving, turning, and breaking soil. According to agronomic requirements for grape soil clearing, the scraper surface had a processing width of 1400 mm, a height of 560 mm, a thickness of 10 mm, and a scraper processing width of 65 mm. However, since the change of bulldozing angle γ (the angle between the scraper and the unit's forward direction), cutting angle δ (the angle between the scraper and the ground), and turning angle β (the angle between the top edge of the scraper and the horizontal plane) had the most critical influence on the shape of the earth contact surface and the operating state, γ, δ, and β were selected as the optimization parameters of the scraper.

2.1.3 Structure of the rotary blade

The rotary blade in the prototype consists primarily of a scimitar, a cutter head, a cutter shaft, and a cutter holder, as shown in Figure 3. During operation, the rotary blade moves uniformly in a straight line at the forward speed v_m, driven by the traction force generated by the tractor, while simultaneously engaging in circular motion at a speed n_r, powered by the hydraulic device. Consequently, the soil at the bottom of the ridge rotates toward the vineyard passage.

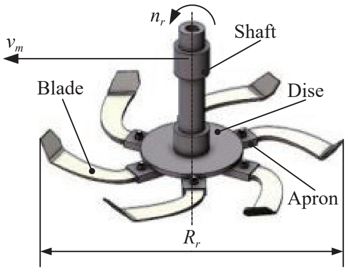

Figure 3 Structural diagram of the rotary blade

According to the Chinese national standard GB/T 5669-2008, the grape soil-clearing operation is the initial cultivation of untilled soil, specifically in vineyard soil with dry sandy loam characteristics. In this paper, the IT260-type wide curved rotary blade was chosen for the task. The tool shaft had a machining diameter of 50 mm, and the tool holder's processing dimensions were 64 mm in length, 51 mm in width, and 21 mm in thickness. However, the difference in rotational speed n_r, rotational radius R_r, and quantity Z_r of the rotary tillage tool had a noticeable influence on its motion trajectory, which further affected the operation effect of the rotary tillage tool. Therefore, n_r, R_r, and Z_r were identified as parameters requiring optimization for the rotary blade.

2.1.4 Structure of the flexible brush

The flexible brush in the prototype mainly comprises a plastic wire brush, mixed wire brush, brush shaft, cylinder, square tube, and bottom plate, as shown in Figure 4. The brush shaft and square tube were bolted and welded onto the cylinder, while the plastic wire brush and mixed wire brush were pressed onto the square tube from the bottom to the top. A base plate was welded to the cylinder to secure the brushes. During operation, the flexible brush moved uniformly in a linear motion at a speed of v_m. Simultaneously, the hydraulic device drove the brush to make a circular motion at speed n_b, which threw the soil brush at the ridge and vine part to the row.

During the flexible brush operation, the top of the brush easily came into contact with the grapevine. To minimize potential damage, the top brush was made of pure plastic bristles (2.8 mm in diameter). The bottom of the flexible brush was more prone to friction with the ground, so it was composed of a mixture of plastic bristles and steel wire (0.7 mm galvanized steel wire) to enhance durability and reduce wear. Compared with the flat brush, the concave and convex brush (with a height of 40 mm per segment) was chosen to better conform to the soil ridges formed after the scraper and rotary tilling knife operations. Additionally, to prevent the brush from hitting the cement frame pole and prolong its lifespan, a safety gap of W_{pb}=50 mm was maintained between the pole and the brush.

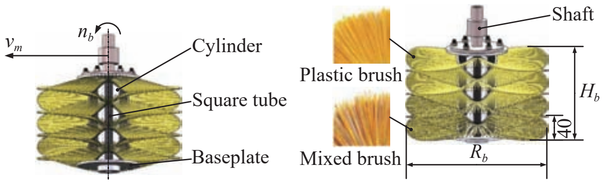

a. Axonometric diagram b. Axonometric diagram

Figure 4 Structural diagram of the flexible brush

However, variations in the flexible brush's speed (n_b), gyration radius (R_b), and number of brushes (Z_b) significantly impacted its movement trajectory and working height, thereby affecting its overall performance. As a result, n_b, R_b, and Z_b were identified as the key parameters to be optimized for the flexible brush.

2.2 Discrete element model

2.2.1 Contact model and model parameter selection

In this study, the discrete element model of soil ridges and soil-clearing components of grapevine was established by selecting the contact model of soil particles and model parameters[33]. The grape production and planting areas in China's Ningxia region primarily consist of sandy loam soil with high moisture content and firm texture. Consequently, the Edinburgh Elasto-Plastic Adhesion Model (EEPA) was chosen to accurately describe this specific sandy loam soil[34,35]. Soil, 65Mn spring steel, and PTEE plastic were the primary materials of soil ridge and soil-clearing parts of grapevine. Referring to relevant literature[36-38], the mechanical properties and contact parameters of the materials were determined, and the Hertz-Mindlin anti-slip model was used to describe the relationship between 65Mn, PTEE, and soil.

The simulation accuracy and calculation efficiency were comprehensively considered in this paper. The single spherical structure was preferred in the operation of the machine, and the 0.5 diameter was filled with 30%, 1.0 diameter was filled with 40%, and 1.5 diameter was filled with 30%[39]. In addition, based on the configuration parameters of the EEPA contact model, the time step recommended by the EDEM software was adopted and the relevant solver and simulation hardware were selected. The parameters of the discrete element model are listed in Tables 2-4.

Table 2 User-defined particle size distribution parameters

Input parameter	Value
0.5 scale by radius	30%
1.0 scale by radius	40%
1.5 scale by radius	30%

Table 3 Materials mechanical properties parameters

Input parameter	Poisson's ratio	Density/ $kg\cdot cm^{-3}$	Shear modulus/ Pa	Particle shape	Particle radius/ mm
Soil particle properties	0.36	2130	9.6×10^5	Single sphere	6.5
65Mn properties	0.3	7865	7.9×10^{10}	-	-
PTEE properties	0.4	2100	1.0×10^8	-	-

2.2.2 DEM of soil ridge

The parameter optimization simulation experiments were conducted based on a discrete elemental model of grapevine buried soil ridges. To obtain the specific dimensions of the buried soil ridge sections of the grapevine, a DJI Phantom 4 UAV was utilized to capture images of the soil ridges. Four survey lines and three section locations (Line 1, Line 2, and Line 3) were chosen, resulting in a total of 12 measurement points. Elevation images of the corresponding sections were taken, and each measurement point was labeled from east to west. The soil ridges were irregularly shaped, so they were approximated as trapezoids to obtain the main parameters of the cross-section, including the ridge height *h*, the width of the upper base *a*, and the width of the lower base *b*. The profile curves were extracted from the elevation maps and imported into the AutoCAD software to perform the measurement statistics. The measurement process is shown in Figure 5.

Due to inconsistent land flatness in the vineyard, the bottom of the two rows of soil ridges on the east side (i.e., measurement points 1, 2, 5, 6, 9, and 10) was based on an altitude of 1054.1 m. In comparison, the bottom of the two rows of soil ridges on the west side (i.e., measurement points 3, 4, 7, 8, 11, and 12) was based on an altitude of 1054 m. The measurement results are listed in Table 5.

All models were created in a soil tank measuring 9000 mm×5000 mm×500 mm, constructed according to the relevant dimensional parameters based on the agronomic characteristics of grape soil clearing in the Ningxia region of China, using the Geometry command. The cement frame rod, steel wire frame, and drip irrigation pipe were all made of 65Mn and modeled using the Box and Cylinder commands in Geometry. During the soil ridge modeling process, grape vines were omitted, and a particle factory was created using the Polygon command in Geometry, allowing soil particles to be dropped freely at an initial speed of 2 m/s. Finally, a soil ridge model with a total amount of 1 300 000 particles and a length of 4000 mm was formed. The cross-sectional dimensions of the soil ridge model were as follows: height *h*=425 mm, top width *a*=750 mm, and bottom width *b*=2000 mm. The soil ridge model is shown in Figure 6.

Table 4 Intermaterial contact parameters

Input Parameter	Value
Edinburgh elasto-plastic adhesion interactions among the soil particles	
Coefficient of restitution	0.58
Coefficient of static friction	0.67
Coefficient of rolling friction	0.52
Surface energy/J·m^{-2}	26.3
Contact plasticity ratio	0.31
Slope exp	1.5
Tensile exp	4
Tangential stiff multiplier	0.39
Particle radius/mm	6.5
Hertz-Mindlin interactions between the soil and 65Mn	
Coefficient of restitution	0.50
Coefficient of static friction	0.30
Coefficient of rolling friction	0.10
Hertz-Mindlin interactions between the soil and PTEE	
Coefficient of restitution	0.60
Coefficient of static friction	0.52
Coefficient of rolling friction	0.045
Simulator settings	
Time step/s	4.12×10^{-5}
Data save interval/s	0.05
CUDA engine device	Tesla P40
Solver precision	Double

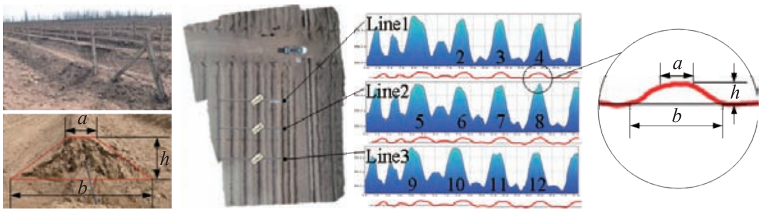

a. Shape of ridges. b. Selection of rows and points for soil ridge measurement c. Acquisition of image data of the cross-sectional elevation of the soil mound at the measurement point d. Extraction of cross-sectional dimensions of measurement points

Figure 5 Dimension measurement of ridge cross-section profile

Table 5 Measurement results of cross-section of soil ridge

Measurement size	Line 1				Line 2				Line 3				Average
	1	2	3	4	1	2	3	4	1	2	3	4	
h/mm	428	381	455	412	394	356	479	466	416	409	432	459	424
a/mm	933	795	640	706	926	751	717	725	739	746	785	692	763
b/mm	2242	1754	2013	2089	2201	1848	2238	1996	2118	1999	2169	2036	2059

2.3 Test procedure and test factors

The parameter optimization of each soil-clearing component was achieved by simplifying the model of the scraping-rotating-brushing dehilling machine and utilizing SolidWorks 3D modeling software in conjunction with EDEM discrete element simulation software to set the parameters. Due to the various influencing factors involved in the clearing components, optimizing the whole machine was relatively tricky. The scraper model, the scraping-rotating combined model (the combination of the scraper and the rotary blade), and the scraping-rotating-brushing combined model (the combination of the scraper, the rotary blade, and the clearing brush) were respectively used to carry out the parameter optimization simulation tests of the scraper, the rotary blade, and the brush, and to determine the optimum structural parameters of the scraper, rotary clearing tool, and clearing brush, respectively. The model and test flow of soil-clearing components are shown in Figure 7.

The key factors affecting the performance of each soil-clearing component were selected as test variables. The test design methods used include the single-factor test, second-order central composite design, and orthogonal test[40,41], which were applied to conduct parameter optimization simulations for each soil-clearing component.

The single-factor test factors of each soil cleaning part are listed in Table 6. The factors for the secondary center combination test of the scraper are listed in Table 7. The orthogonal test factors of the rotary blade are listed in Table 8. The orthogonal test factors of the flexible brush are listed in Table 9.

2.4 Simulation experiment of scraper parameter optimization

2.4.1 Single-factor test

The operational process of the scraper in the dehilling machine was analyzed, and a vector map of soil velocity during scraper operation at various levels of each factor was plotted, as shown in Figure 8.

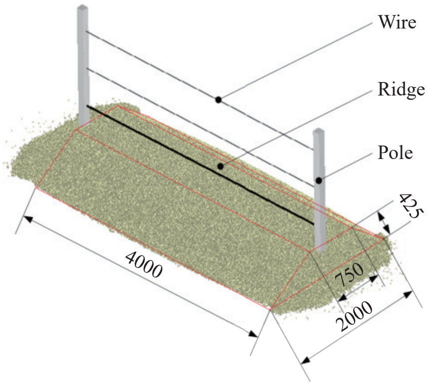

Figure 6 DEM of soil ridge

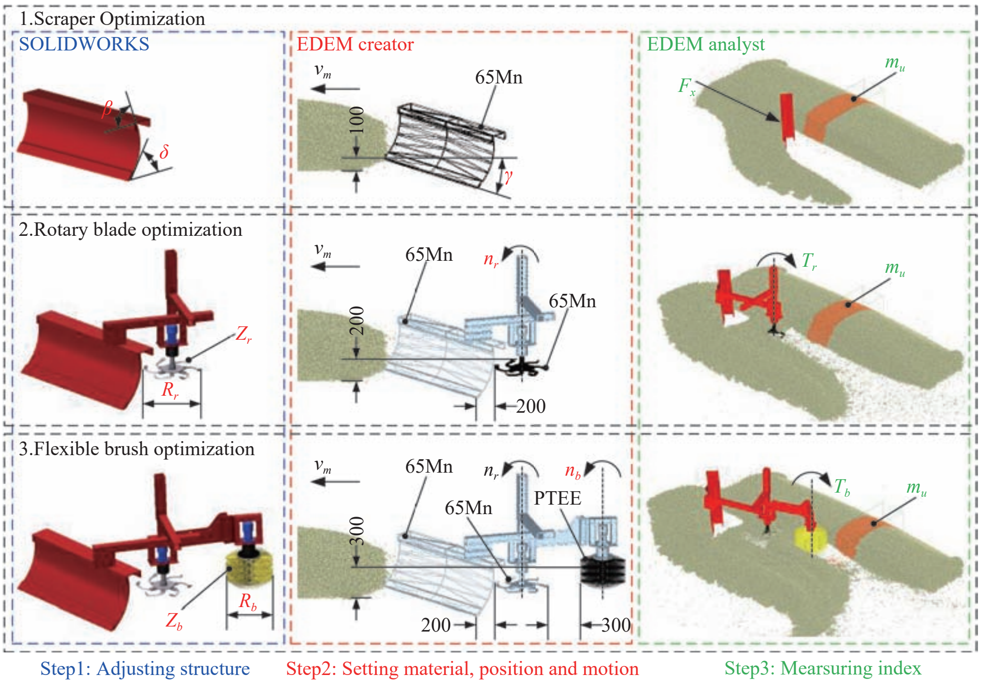

Figure 7 Flow chart of simulation test for model simplification and parameter optimization

Table 6 Single-factor test of each factor level

Level	Scraper			Rotary blade			Flexible brush		
	γ/(°)	δ/(°)	β/(°)	n_r/r·min^{-1}	R_r/mm	Z_r	n_b/(r·min^{-1})	R_b/mm	Z_b
1	30	30	45	280	260	2	300	250	6
2	38	40	53	335	280	3	363	275	7
3	45	50	60	390	300	4	425	300	8
4	53	60	68	445	320	5	488	325	9
5	60	70	75	500	340	6	550	350	10

Table 7 Levels of various factors in the scraper secondary center combination test

Coded value	γ/(°)	δ/(°)	β/(°)
–1.682	30	40	45
–1	36	46	51
0	45	55	60
1	54	64	69
1.682	60	70	75

Initially, the soil quality was assessed within the measurement area both before and after the scraper operation, and subsequently the soil-clearing rate C_m was computed. Next, a time-dependent curve was constructed for illustrating the horizontal forward resistance of the scraper. The average horizontal resistance F_x during the smooth operating phase was calculated. Lastly, the impact trend of each factor on the indicators C_m and F_x was analyzed to identify the optimal range of values for each factor when fine-tuning the scraper parameters.

Table 8 The level of each factor in the orthogonal test of rotary tilling knife

Level	n_r/(r·min^{-1})	R_r/mm	Z_r
1	335	260	2
2	376	280	3
3	418	300	4
4	459	320	5
5	500	340	6

Table 9 Level of factors in the flexible brush orthogonal test

Level	n_b/(r·min^{-1})	R_b/mm	Z_b
1	300	250	6
2	363	275	7
3	425	300	8
4	488	325	9
5	550	350	10

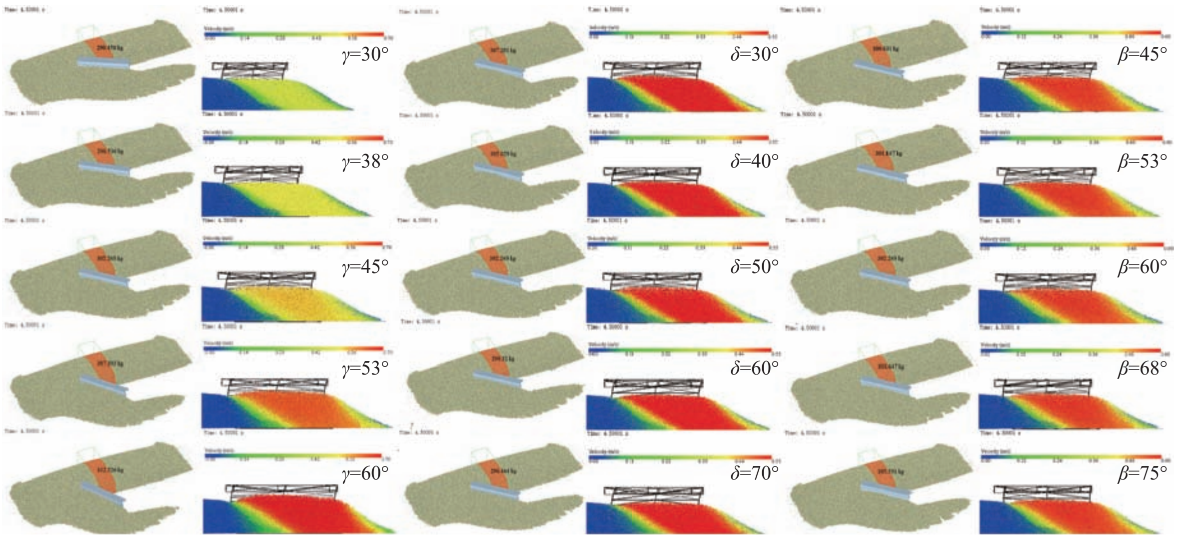

a. Operation process simulation diagram at different bulldozing angles　b. Velocity vector diagram at different bulldozing angles　c. Operation process simulation diagram at different cutting angles　d. Velocity vector diagram at different cutting angles　e. Operation process simulation diagram at different turning angles　f. Velocity vector diagram at different turning angles

Figure 8　Simulation process of the scraper

2.4.2　Quadratic regression center combination test

To obtain the optimal combination of scraper parameters, an optimization simulation test scheme was designed using a quadratic regression central composite design in Design Expert 11 software[42]. Subsequently, an analysis of variance (ANOVA) on the test data was conducted, the regression equations were derived for the test metrics and factors through quadratic regression fitting, and-response surface analysis was performed on these equations. Ultimately, the optimal solution was determined by considering both the constraints of the factors and the desired objective values of the test metrics.

2.5　Simulation experiment of rotary blade optimization

2.5.1　Single-factor test

The operation process of the rotary blade of the dehilling machine was analyzed, and the vector map of soil velocity for rotary blade operation at different levels of each factor was plotted. The simulation process is shown in Figure 9.

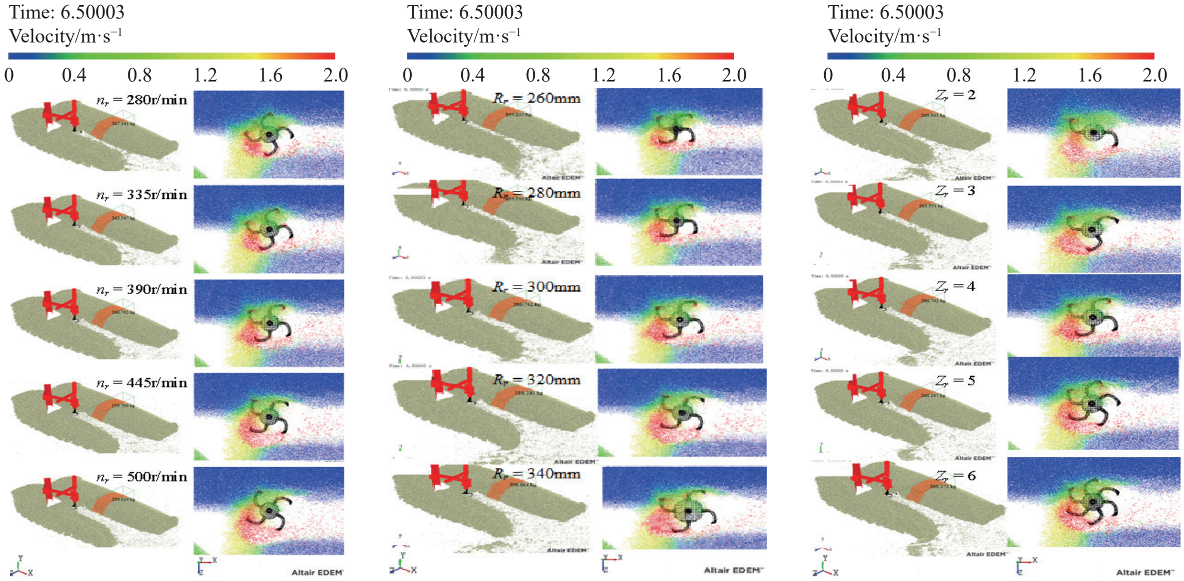

a. Operation process simulation diagram at different rotary blade speed　b. Velocity vector diagram at different rotary blade speed　c. Operation process simulation diagram at different rotary blade gyration radius　d. Velocity vector diagram at different rotary blade gyration radius　e. Operation process simulation diagram at different rotary blade numbers　f. Velocity vector diagram at different rotary blade numbers

Figure 9　Simulation process of rotary blade

In the initial phase, the soil quality in the measurement area before and after the rotary blade operation was also assessed by quantifying the soil-clearing rate C_m. Then the torque curve of the rotary blade over time was charted and the average torque value T_r during operation was calculated. Finally, the influence of each factor on the indicators C_m and T_r was scrutinized to determine the optimal range of each factor in the optimization of rotary blade parameters.

2.5.2　Orthogonal test

To further obtain the optimal combination of rotary blade parameters, we employed three-factor, five-level orthogonal experiments to design the simulation test scheme for parameter optimization. We carried out range analysis on the experimental data to derive the sequence of influence of each factor on the experimental indices, and the significance of the influence of each factor on the indices was obtained by ANOVA. Finally, through the combined weighted scoring method and range analysis method, we obtained the combined influence sequence of each factor and the optimal combination parameters.

In this context, a comprehensive weighted scoring method was employed, guided by the principle that a lower rotary blade torque T_r and a higher soil-clearing rate C_m were desirable, aiming for a balance between the two. The weighting scheme involved assigning a weight of –0.5 (W_{T_r}) to torque and 0.5 (W_{C_m}) to the soil-clearing rate. Utilizing Equation (1), the comprehensive weighted scores for the indicators were calculated.

$$Q_N = Q_{T_r} + Q_{C_m} = W_{T_r}\frac{100}{T_{rM}-T_{rm}}(T_{ri}-T_{rm}) + W_{C_m}\frac{100}{C_{mM}-C_{mm}}(C_{mi}-C_{mm}) \tag{1}$$

2.6 Simulation experiment of flexible brush parameter optimization

2.6.1 Single-factor test

The operation process of the flexible brush of the dehilling machine was analyzed, and the vector map of soil velocity for flexible brush operation at different levels of each factor was plotted. The simulation process is shown in Figure 10.

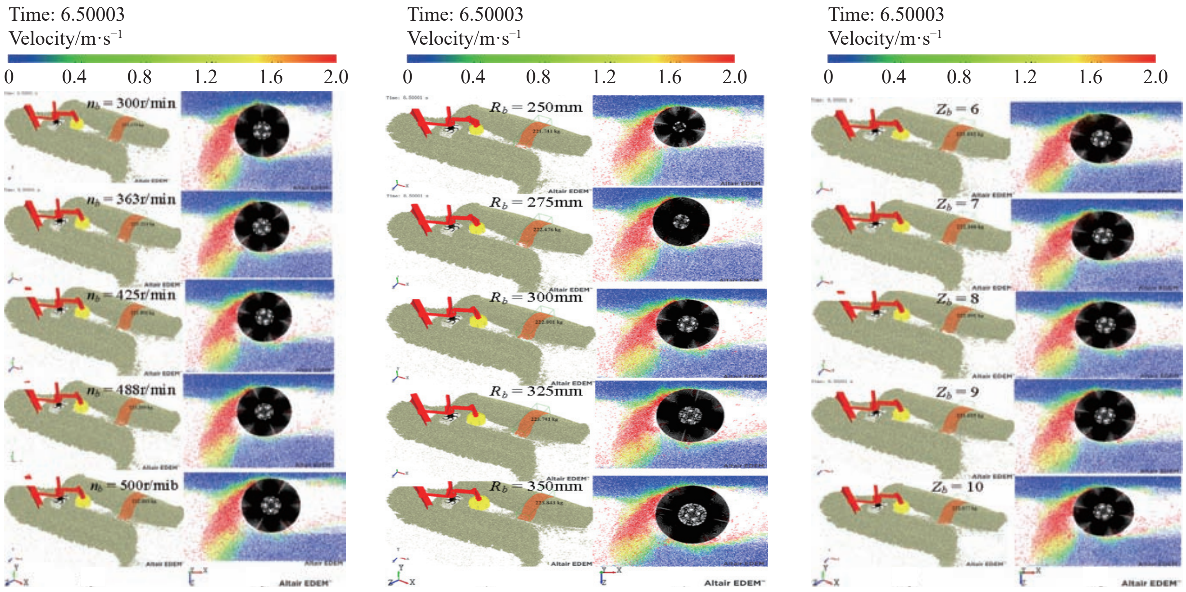

a. Operation process simulation diagram at different flexible brush speed
b. Velocity vector diagram at different flexible brush speed
c. Operation process simulation diagram at different flexible brush gyration radius
d. Velocity vector diagram at different flexible brush gyration radius
e. Operation process simulation diagram at different flexible brush numbers
f. Velocity vector diagram at different flexible brush numbers

Figure 10 Simulation process of flexible brush

Firstly, the soil in the measurement area before and after the flexible brush operation was weighted, and the soil-clearing rate C_m was calculated. Then, the torque of the flexible brush curve graph over time was plotted, and the average value of the torque T_b was calculated. Finally, the trend of the influence of each factor on the indicators C_m and T_b was analyzed, and the appropriate range of each factor was determined in the optimization of parameters of the flexible brush.

2.6.2 Orthogonal experiment

To identify the optimal combination of parameters for the flexible brush, this paper utilized a three-factor, five-level orthogonal test to design a simulation test program for parameter optimization. A polar analysis of the test data was conducted to determine the influence order of each factor on the test indices. The significance of each factor’s influence was assessed through analysis of variance (ANOVA), and the comprehensive influence order was derived using the integrated weighted scoring method, polar analysis, and the identification of optimal combination parameters.

Among them, the integrated weighted scoring method was applied based on the principle of minimizing the flexible brush torque T_b and maximizing the soil-clearing rate C_m, while achieving a balance between the two. The torque was assigned a weight of –0.5 (W_{T_b}), and the soil-clearing rate was assigned a weight of 0.5 (W_{C_m}). The integrated weighted score of the indicators was calculated using Equation (2).

$$Q_N = Q_{T_b} + Q_{C_m} = W_{T_b}\frac{100}{T_{bM}-T_{bm}}(T_{bi}-T_{bm}) + W_{C_m}\frac{100}{C_{mM}-C_{mm}}(C_{mi}-C_{mm}) \tag{2}$$

2.7 Field trials

This study selected the wine grape planting base at Yuquanying Farm in Ningxia, China, as the experimental site. The soil removal rate was used as the test index, and the scraping-rotating dehilling machine and the scraping-rotating-brushing dehilling machine were chosen as the test subjects. The experimental design included a 50-cm soil ridge measurement area. The soil weight at three stages was measured: the original soil ridge, the soil ridge after the operation of the scraping-rotating dehilling machine, and the soil ridge after the operation of the scraping-rotating-brushing dehilling machine. The scene is illustrated in Figure 11.

3 Results and discussion

3.1 Simulation result of scraper

3.1.1 Single-factor simulation results

Figures 12a and 12b show that as the bulldozing angle increases, the velocity of soil particles ahead of the scraper rises, leading to an augmented horizontal forward resistance and a subsequent reduction in the soil removal rate. When the bulldozing angle exceeded 52.5°, the soil removal rate dropped below 45%. To

a. Scraping-rotating grape soil clean machine field operation site

b. Scraping-rotating-brushing dehilling machine field operation site

c. Original scene

d. Scraping-rotating soil clean machine operating effect

e. Scraping-rotating-brushing dehilling machine operating effect

Figure 11 Measurement site

enhance the scraper's working width, increase the distance for soil movement to the row, and ensure the smooth operation of subsequent cleaning components, preventing soil particles from ascending along the scraper and passing over its top, it was advisable to use a larger bulldozing angle. Conversely, to reduce the horizontal resistance of the scraper and improve soil removal efficiency, a smaller bulldozing angle should be selected. Thus, the bulldozing angle should be minimized, while ensuring that soil particles do not pass over the scraper, to maintain the normal operation of the soil-clearing components.

Figures 12c and 12d show that when the cutting angle was below 40°, an increase in the cutting angle results in an augmented bottom curvature of the scraper. This curvature made it difficult for soil particles to rise along the scraper, resulting in decreased particle accumulation in front of the scraper, a reduction in the overall force exerted by the scraper, and a subsequent decrease in horizontal forward resistance. Conversely, when the cutting angle surpassed 40°, an increase in the cutting angle enlarges the clearing area of the scraper, resulting in a higher volume of soil being moved. This led to an overall increase in the force applied by the scraper, accompanied by a simultaneous rise in both horizontal resistance and soil removal rate.

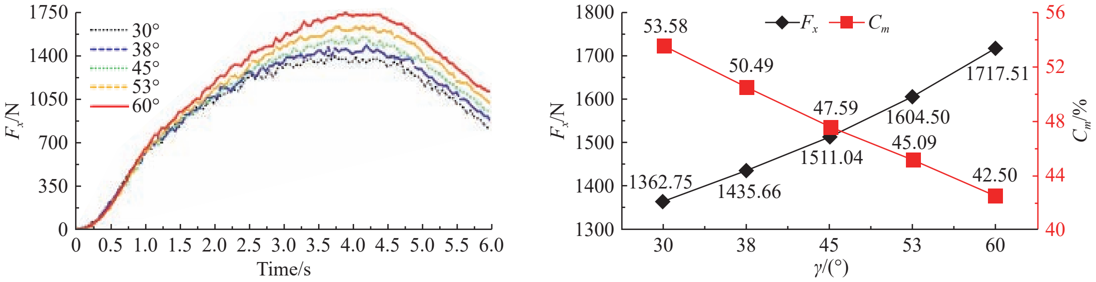

a. Forward resistance diagram under the influence of bulldozing angle

b. Trend diagram under the influence of bulldozing angle

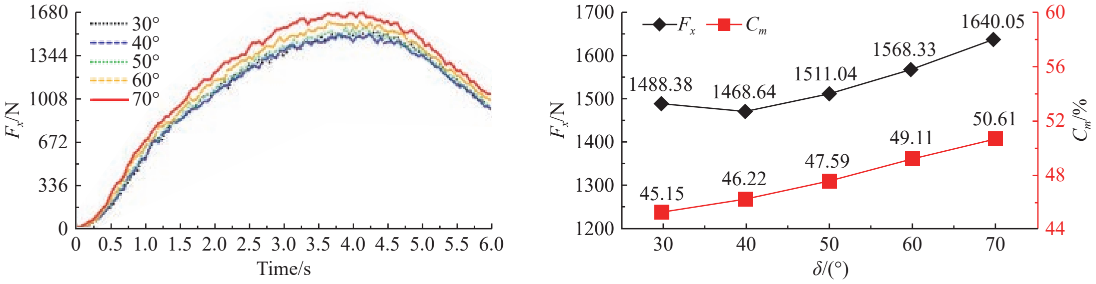

c. Forward resistance diagram under the influence of cutting angle

d. Trend diagram under the influence of cutting angle

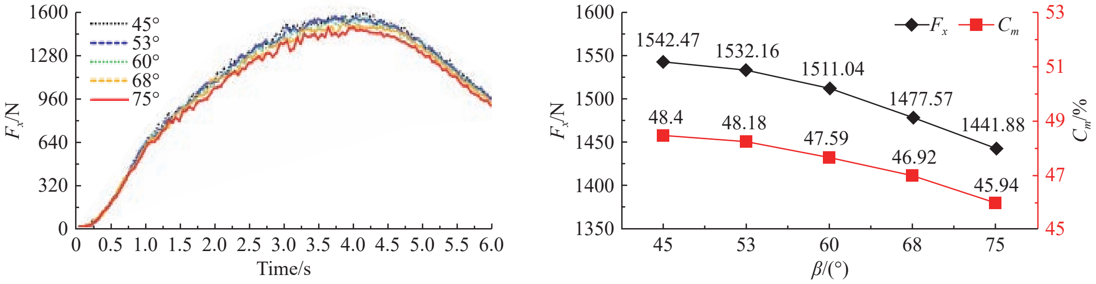

e. Forward resistance diagram under the influence of turning angle

f. Trend diagram under the influence of turn angle

Figure 12 Scraper single-factor simulation results

Figures 12e and 12f ereveal that with the increase of the turning angle, the clearing area of the scraper decreased, resulting in a decrease in the amount of soil extracted by the scraper. This reduction in soil accumulation in front of the scraper led to an overall decrease in the force applied by the scraper, consequently lowering both horizontal forward resistance and soil removal rate. Therefore, the selection of the turning angle should strike a balance between horizontal forward resistance and soil removal rate.

In summary, this paper determined the value range of each factor of the scraper. The bulldozing angle was 30°-60°, the cutting angle was 40°-70°, and the front turning angle was 45°-75°.

3.1.2 Quadratic regression center combination test results

The Design Expert software was employed to conduct a simulation test using the three-factor and five-level central composite design. The test results were recorded with precision up to two decimal places, as listed in Table 10.

Table 10 Results of secondary center combination test of scraper

Serial number	Coding values of each factor			Test indicators	
	A-γ	B-δ	C-β	F_x/N	C_m/%
1	–1	–1	–1	1430.18	51.50
2	1	–1	–1	1614.74	44.30
3	–1	1	–1	1430.90	51.65
4	1	1	–1	1833.46	48.43
5	–1	–1	1	1397.30	50.40
6	1	–1	1	1525.48	42.19
7	–1	1	1	1401.57	51.18
8	1	1	1	1769.52	47.21
9	–1.682	0	0	1346.61	53.20
10	1.682	0	0	1808.77	44.18
11	0	–1.682	0	1469.27	46.22
12	0	1.682	0	1638.10	50.61
13	0	0	–1.682	1561.35	49.05
14	0	0	1.682	1477.55	46.89
15	0	0	0	1530.49	48.38
16	0	0	0	1532.65	48.45
17	0	0	0	1544.93	48.62
18	0	0	0	1549.68	48.77
19	0	0	0	1528.54	48.30
20	0	0	0	1538.78	48.53

Regression significance analysis was performed on the test results in the table, and the results are listed in Table 11. As shown in Table 11, the horizontal forward resistance F_x and soil removal rate C_m models had p<0.01, and the regression model misfit terms had p>0.05. This indicates that the regression models for horizontal forward resistance and soil-clearing rate were highly significant, while the misfit terms were insignificant. Therefore, the regression models fit the data well, confirming their validity. For the horizontal forward resistance model, the effects of A, B, C, AB, AC, and A^2 regression terms were highly significant ($p\leq 0.01$); the effects of B^2 and C^2 regression terms were significant ($0.01<p\leq 0.05$); the effects of BC regression terms were not significant; and the effects of each factor on horizontal forward resistance were in the following order of precedence: $A>B>C$.

Table 11 Significance analysis of regression model for secondary center combined test of scraper

Source of square	F_x				C_m			
	Sum of variance	DoF	F value	p value	Sum of variance	DoF	F value	p value
Model	3.356E+05	9	554.63	< 0.0001**	141.86	9	682.04	< 0.0001**
A-γ	2.535E+05	1	3770.17	< 0.0001**	104.46	1	4519.84	< 0.0001**
B-δ	41 373.62	1	615.42	< 0.0001**	22.33	1	966.22	< 0.0001**
C-β	9297.98	1	138.30	< 0.0001**	5.33	1	230.68	< 0.0001**
AB	26 194.17	1	389.63	< 0.0001**	8.45	1	365.46	< 0.0001**
AC	1034.90	1	15.39	0.0029**	0.3872	1	16.75	0.0022**
BC	104.18	1	1.55	0.2416	0.2888	1	12.50	0.0054**
A^2	2851.66	1	42.42	< 0.0001**	0.0627	1	2.71	0.1305
B^2	448.69	1	6.67	0.0273*	0.0141	1	0.6091	0.4532
C^2	613.40	1	9.12	0.0129*	0.5125	1	22.18	0.0008**
Residual	672.28	10			0.2311	10		
Lack of Fit	314.14	5	0.8772	0.5554	0.0864	5	0.5973	0.7072
Pure error	358.14	5			0.1447	5		
Cor total	3.363E+05	19			142.09	19		

Note: * represents factor with a highly significant influence on the index ($0.01<p\leq 0.05$); ** represents factor with a significant influence on the index ($p\leq 0.01$).

In the soil removal rate model, the regression terms A, B, C, AB, AC, BC, and C^2 showed a highly significant impact ($p\leq 0.01$). However, the regression terms A^2 and B^2 did not have a significant impact. The influence of factors on soil removal rate can be ranked in the following order: $A > B > C$.

Response surface plots of the effect of each test factor on horizontal forward resistance and removal rate were obtained using Response Surface Methodology, as shown in Figure 13.

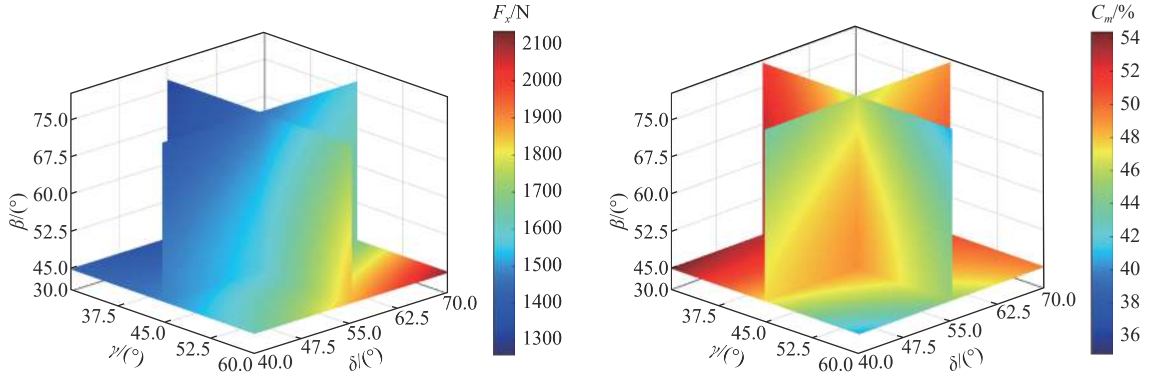

a. Horizontal forward resistance F_x b. Soil removal rate C_m

Figure 13 Effects of bulldozing angle γ, cutting angle δ, and forward turning angle β on horizontal forward resistance F_x and soil removal rate C_m of scraper

Figure 13 shows that an increase in the pushing angle and cutting angle resulted in an increase in the horizontal forward resistance of the scraper. With the increase of the front turning angle, the horizontal forward resistance of the scraper decreased. The soil removal rate decreased as the pushing and turning angles increased. However, the soil removal rate increased as the cutting angle increased. Therefore, to obtain a low horizontal forward resistance F_x, the bulldozing angle γ and cutting angle δ of the scraper should not be too large, and the turning angle β should not be too small. To obtain a higher soil removal rate C_m, the scraper bulldozing angle γ and turning angle β should not be too large, and the cutting angle δ should not be too small.

Under the condition that the designed soil removal rate was 45%, with the objective of reducing the horizontal forward resistance of the scraper, the multi-objective variable optimization method was used combined with Design Expert 11 software to optimize and solve the test index model. Aiming at the lowest horizontal forward resistance F_x and soil removal rate C_m = 45%, a mathematical model was developed for planning the structural parameters of the scraper under the constraint conditions of scraper pushing angle γ, cutting angle δ, and forward turning angle β, as shown in Equation (3).

$$\begin{cases} \min F_x(\gamma,\delta,\beta) \\ C_m(\gamma,\delta,\beta) = 45 \\ 30 \le \gamma \le 60 \\ 40 \le \delta \le 70 \\ 45 \le \beta \le 60 \end{cases} \tag{3}$$

3.1.3 Parameters for the optimum combination of scraper

The optimal parameter combinations obtained using the optimized numerical module of Design Expert 11 software were as follows: the bulldozing angle was 44°, the cutting angle was 40°, and the front turning angle was 75°. At this time, the horizontal forward resistance of the scraper predicted by the model was 1395.54 N, and the soil removal rate was 45%. Simulation verification was carried out according to the optimized results, and the effect of the simulation operation is shown in Figure 14.

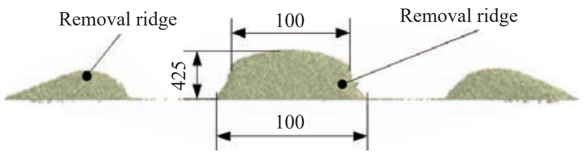

Figure 14 Optimal parameter combined scraper simulation results

3.2 Simulation result of rotary blade

3.2.1 Single-factor simulation results

Figures 15a and 15b demonstrate that an augmentation in the rotary speed of the rotary blade resulted in a decrease in soil quality in the test area, which led to an increase in the soil removal rate and the distance between rows (i.e., throw distance) where the rotary blade throws the soil. The increase in speed also reduced the cutting distance and the average pressure in the normal direction of the rotary blade, which reduced the torque of the rotary blade, and this torque stabilized at rotary blade speeds greater than 445 r/min. Simultaneously, as the rotational speed increased, the soil leakage width decreased while the soil removal rate increased, stabilizing when the rotational speed exceeded 390 r/min. Therefore, to ensure enough soil throwing distance, reduce torque of the rotary blade, and improve soil removal rate, the rotation speed of the rotary blade should be selected with a large value.

Figures 15c and 15d demonstrate that as the rotary radius of the blade increased, both the torque of the rotary blade and the soil removal rate increased, thereby extending the soil throwing distance. The torque increased significantly when the rotary radius of the rotary tiller was in the range of 260-300 mm. When the rotary radius of the rotary blade was greater than 300 mm, the torque increase gradually tended to be stable. Increasing the rotary radius of the rotary blade would effectively increase the soil removal rate

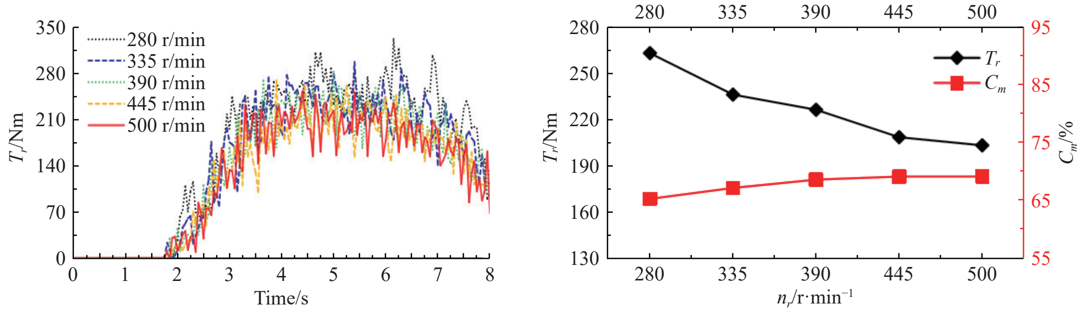

a. Torque curve diagram under the influence of rotational speed
b. Trend diagram under the influence of rotational speed

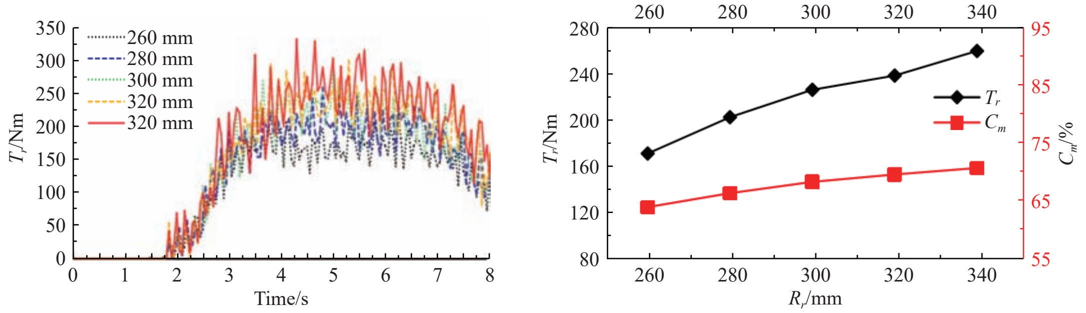

c. Torque curve diagram under the influence of gyration radius
d. Trend diagram under the influence of gyration radius

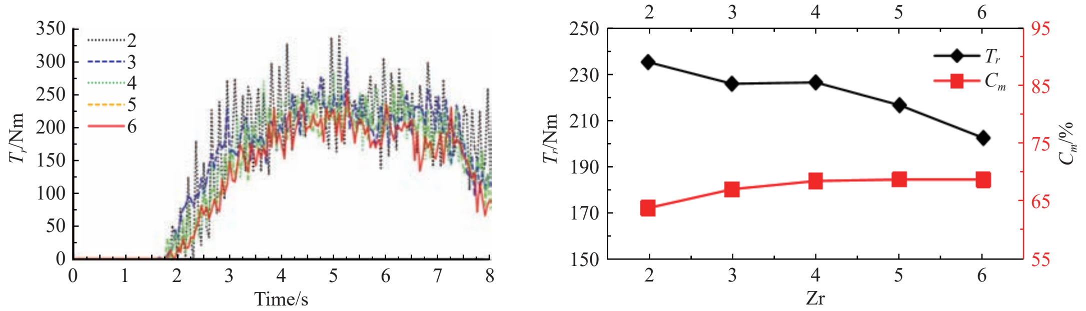

e. Torque curve diagram under the influence of the number of blades
f. Trend diagram under the influence of the number of blades

Figure 15 Rotary blade single-factor simulation results of the rotary blade, but it would also increase the contact area and friction between the tool and the soil, resulting in an increase in rotary blade torque. Therefore, selection of a rotary gyration radius should balance the torque and soil removal rate.

Figures 15e and 15f reveal that, as the number of blades increased, the rotary blade torque first decreased, then stabilized, and subsequently gradually declined, exhibiting an overall decreasing trend. This was due to the reduction in normal pressure caused by the decrease in soil cutting advance, which in turn reduced the torque. The increase in the number of blades also reduced the leakage clearing soil width of the rotary blade, thereby increasing the clearing volume and improving the soil removal rate. However, when the leakage clearing soil width was sufficiently small, the clearing volume was basically unchanged, and thus the soil removal rate of the rotary blade first rose and then tended to stabilize with the increase in the number of blades. Therefore, to reduce the torque and increase the distance of throwing soil and the rate of soil removal, the number of blades should be a larger value.

In summary, this paper determined the range of values for each factor of the rotary blade: the rotational speed of the rotary blade was 335-500 r/min, the gyration radius of the rotary blade was 260-340 mm, and the number of blades was 2-6.

3.2.2 Orthogonal test results

As can be seen from Tables 12 and 13, the order of influence of all factors on the comprehensive performance of the rotary blade was as follows: $C>A>B$. The optimal combination parameter was $A_5B_3C_5$, that is, the rotational speed of the rotary blade was 500 r/min, the rotary radius of the rotary blade was 300 mm, and the number of blades was 6. The simulation operation was carried out according to the optimized results, and the effect is shown in Figure 16. At this time, the torque of the rotary blade was172.69 N·m, and the soil removal rate was 69.68%.

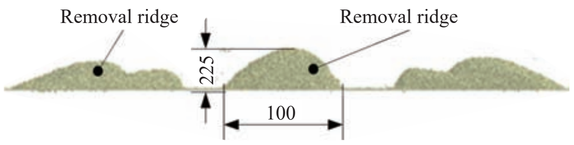

Figure 16 Simulation effect of the combination of rotary blade and scraper with optimal parameters

3.3 Simulation result of soil flexible brush

3.3.1 Single-factor simulation results

Figures 17a and 17b show that an increase in the speed of the flexible brush would cause the torque of the flexible brush to decrease and then increase and then decrease again, and the soil removal rate to increase and then decrease and then increase again. Therefore, consideration should be given to balancing the torque of the flexible brush with the rate of soil removal when selecting the speed of the flexible brush.

Figures 17c and 17d show that as the radius of gyration of the flexible brush increased, the brush torque increased, and the soil removal rate decreased. Therefore, the gyration radius of the flexible brush should be selected as a small value.

Figures 17e and 17f illustrate an increase in the torque of the flexible brush as the number of brushes increased, while the soil removal rate remained relatively constant. Thus, it was advisable to opt for a smaller number of brushes.

In summary, this paper establishes the range of values for each factor related to the flexible brush: the speed of the flexible brush is between 300 r/min and 550 r/min, the gyration radius is between 250 mm and 350 mm, and the number of brushes ranges from 6 to 10.

Table 12 Orthogonal test results and range analysis of rotary blade

Serial No.	Level						Index		
	A-n_r	B-R_r	C-Z_r	Blank	Blank	Blank	T_r/(r·min^{-1})	C_m/%	Q_N
1	1	1	1	1	1	1	189.54	58.23	–23.12
2	1	2	2	2	2	2	209.31	62.92	–11.00
3	1	3	3	3	3	3	236.00	66.47	–5.48
4	1	4	4	4	4	4	240.90	69.18	3.56
5	1	5	5	5	5	5	240.80	70.42	8.42
6	2	1	2	3	4	5	175.74	61.87	–4.64
7	2	2	3	4	5	1	202.69	65.97	2.95
8	2	3	4	5	1	2	213.87	68.41	8.98
9	2	4	5	1	2	3	216.76	69.68	13.02
10	2	5	1	2	3	4	275.85	66.26	–18.71
11	3	1	3	5	2	4	168.55	64.34	7.23
12	3	2	4	1	3	5	187.27	66.87	11.26
13	3	3	5	2	4	1	193.45	69.84	20.91
14	3	4	1	3	5	2	248.88	66.27	–10.27
15	3	5	2	4	1	3	265.02	70.26	0.26
16	4	1	4	2	5	3	150.30	65.35	16.85
17	4	2	5	3	1	4	159.81	66.99	20.28
18	4	3	1	4	2	5	226.66	65.87	–4.91
19	4	4	2	5	3	1	242.66	69.63	4.76
20	4	5	3	1	4	2	249.05	71.06	8.35
21	5	1	5	4	3	2	115.30	64.13	22.99
22	5	2	1	5	4	3	193.05	64.76	1.23
23	5	3	2	1	5	4	208.86	69.03	12.95
24	5	4	3	2	1	5	221.24	70.20	13.66
25	5	5	4	3	2	1	234.09	70.64	11.37
T_r K_1	223.31	159.89	226.80	210.30	209.90	212.49			
K_2	216.98	190.43	220.32	210.03	211.07	207.28			
K_3	212.63	215.77	215.51	210.90	211.42	212.23			
K_4	205.70	234.09	205.29	210.11	210.44	210.79			
K_5	194.51	252.96	185.22	211.79	210.31	210.34			
R	28.80	93.08	41.57	1.76	1.52	5.20			
C_m K_1	65.44	62.78	64.28	66.97	66.82	66.86			
K_2	66.44	65.50	66.74	66.91	66.69	66.56			
K_3	67.52	67.92	67.61	66.45	66.67	67.30			
K_4	67.78	68.99	68.09	67.08	67.34	67.16			
K_5	67.75	69.73	68.21	67.51	67.41	67.05			
R	2.34	6.94	3.93	1.06	0.74	0.75			
Q_N K_1	–5.52	3.86	–11.16	4.49	4.01	3.37			
K_2	0.32	4.94	0.47	4.34	3.14	3.81			
K_3	5.88	6.49	5.34	2.25	2.96	5.18			
K_4	9.07	4.95	10.40	4.97	5.88	5.06			
K_5	12.44	1.94	17.12	6.12	6.18	4.76			
R	17.96	4.55	28.28	3.87	3.22	1.80			

Table 13 Variance analysis of rotary blade torque and soil removal rate

Source of square	T_r				C_m			
	Sum of variance	DoF	F value	p value	Sum of variance	DoF	F value	p value
A-n_r	2447.05	4	70.06	<0.0001**	20.88	4	8.74	0.0015**
B-R_r	26 759.15	4	766.17	<0.0001**	161.41	4	67.56	<0.0001**
C-Z_r	5264.98	4	150.75	<0.0001**	52.51	4	21.98	<0.0001**
Error	104.78	12			7.17	12		
Cor total	34 575.95	24			241.96	24		

Note: * represents factor with a highly significant influence on the index ($0.01<p\leq 0.05$); ** represents factor with a significant influence on the index ($p\leq 0.01$).

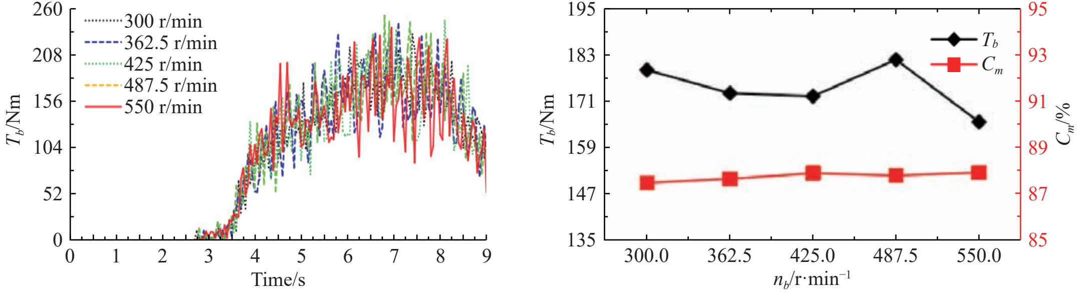

a. Torque curve diagram under the influence of rotational speed

b. Trend diagram under the influence of rotational speed

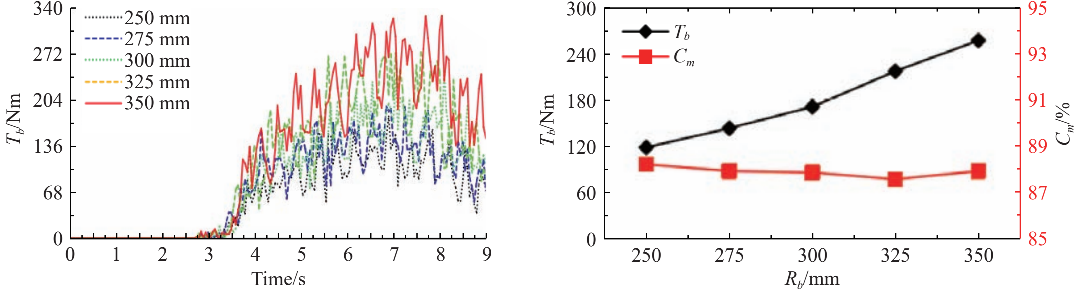

c. Torque curve diagram under the influence of gyration radius

d. Trend diagram under the influence of gyration radius

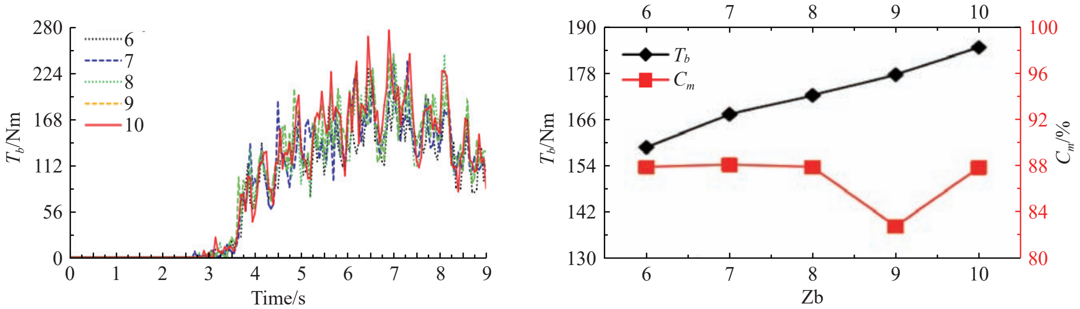

e. Torque curve diagram under the influence of the number of brushes

f. Trend diagram under the influence of the number of brushes

Figure 17 Flexible brush single-factor simulation results

3.3.2 Orthogonal experiment results

This paper employed a three-factor, five-level orthogonal test design to optimize the soil brush parameters in a simulation test program. Polar analysis of the test data was used to determine the order of influence of each factor on the test index. Variance analysis identified the significance of each factor's effect on the index. Finally, the comprehensive influence of the factors and the optimal parameter combination was determined through a weighted scoring method and polar analysis. The simulation test program and results are listed in Table 14.

The order of influence of each factor of clearing brush on torque (T_b) was B>C>A, while the order of influence on clearing rate (C_m) was A>C>B. Variance analysis was performed on the experimental data, and the influence of each factor on both torque (T_b) and clearing rate (C_m) was highly significant, as listed in Table 15.

The effect of each factor on the performance of flexible brushes was comprehensively analyzed, and the results were as follows: B>A>C; the optimal combination parameter was $A_5B_1C_2$, that is, the speed of the flexible brush was 550 r/min; the gyration radius of flexible brush was 250 mm; and the number of brush blades was 7. The simulation operation was carried out according to the optimized results, and the effect is shown in Figure 18. At this time, the torque of the flexible brush was 113.6 N·m, and the soil removal rate was 88.7%.

3.4 Field trials results

The field trials results are listed in Table 16. The table shows that the performance indicators for all types of grape soil removal machines met the required standards. The differences between the actual and simulated test values for the scraping-rotating soil cleaning machine and the scraping-rotating-brushing dehilling machine were 2.47% and 0.05%, respectively, verifying the accuracy of the DEM model.

4 Conclusions

In this study, the structure and operating parameters of the prototype were optimized through simulation tests. A discrete elemental model of grapevine buried ridges and soil-clearing machinery was developed using the discrete elemental method with EDEM 2021.2 software. Taking horizontal forward resistance, torque, and soil removal rate as test indices, the single-factor test was conducted to determine the parameter optimization inverse ranges of each clearing component, and combined with orthogonal test and quadratic center combination test method to derive the optimal combination parameters for the primary working clearing components of the scraping-rotating-brushing dehilling machine. The accuracy of the discrete elemental model was validated through field tests, yielding a relative error of only 0.05%. The application of the discrete elemental method contributes to advancing the mechanization of grape clearing, enhancing efficiency, and

Table 14 Orthogonal test results and range analysis of flexible brushes

	Serial number	Level						Index		
		A-n_b	B-R_b	C-Z_b	Blank	Blank	Blank	T_b/ (r·min^{-1})	C_m/ %	Q_N
	1	1	1	1	1	1	1	108.97	88.11	27.68
	2	1	2	2	2	2	2	140.55	88.00	12.46
	3	1	3	3	3	3	3	179.17	87.49	–22.91
	4	1	4	4	4	4	4	219.55	87.51	–35.19
	5	1	5	5	5	5	5	262.19	87.59	–45.54
	6	2	1	2	3	4	5	110.54	88.28	34.76
	7	2	2	3	4	5	1	147.70	88.05	12.36
	8	2	3	4	5	1	2	182.94	87.91	–5.39
	9	2	4	5	1	2	3	220.79	87.68	–28.01
	10	2	5	1	2	3	4	243.28	88.00	–21.06
	11	3	1	3	5	2	4	119.83	88.26	30.83
	12	3	2	4	1	3	5	144.35	88.19	19.70
	13	3	3	5	2	4	1	184.85	87.87	–7.80
	14	3	4	1	3	5	2	198.90	88.05	–4.35
	15	3	5	2	4	1	3	251.04	88.36	–7.52
	16	4	1	4	2	5	3	123.02	88.23	28.45
	17	4	2	5	3	1	4	143.41	88.13	17.33
	18	4	3	1	4	2	5	157.27	88.21	16.38
	19	4	4	2	5	3	1	193.71	88.27	7.17
	20	4	5	3	1	4	2	255.10	88.54	–0.81
	21	5	1	5	4	3	2	125.43	88.37	33.91
	22	5	2	1	5	4	3	120.14	88.61	46.35
	23	5	3	2	1	5	4	164.45	88.44	24.31
	24	5	4	3	2	1	5	201.38	88.29	5.56
	25	5	5	4	3	2	1	252.33	88.55	0.54
T_b	K_1	182.09	117.56	165.71	178.73	177.55	177.51			
	K_2	181.05	139.23	172.06	178.62	178.15	180.58			
	K_3	179.79	173.74	180.64	176.87	177.19	178.83			
	K_4	174.50	206.87	184.44	180.20	178.04	178.10			
	K_5	172.75	252.79	187.33	175.76	179.25	175.15			
	R	9.34	135.23	21.62	4.44	2.06	5.44			
C_m	K_1	87.74	88.25	88.20	88.19	88.16	88.17			
	K_2	87.98	88.20	88.27	88.08	88.14	88.17			
	K_3	88.15	87.98	88.13	88.10	88.06	88.07			
	K_4	88.28	87.96	88.08	88.10	88.16	88.07			
	K_5	88.45	88.21	87.93	88.13	88.07	88.11			
	R	0.71	0.29	0.34	0.11	0.10	0.10			
Q_N	K_1	–12.70	31.13	13.00	8.57	7.53	7.99			
	K_2	–1.47	21.64	14.24	3.52	6.44	7.16			
	K_3	6.17	0.92	5.01	5.07	3.36	3.27			
	K_4	13.70	–10.96	1.62	3.99	7.46	3.24			
	K_5	22.13	–14.88	–6.02	6.68	3.05	6.17			
	R	34.83	46.00	20.26	5.05	4.49	4.75			

Table 15 Variance analysis of flexible brush torque and soil removal rate

Source of square	T_b				C_m			
	Sum of variance	DoF	F	p	Sum of variance	DoF	F	p
A-n_r	345.25	4	6.85	0.0041**	1.49	4	32.75	< 0.0001**
B-R_r	58 005.07	4	1151.17	< 0.0001**	0.37	4	8.18	0.0020**
C-Z_r	1609.08	4	31.93	< 0.0001**	0.33	4	7.35	0.0031**
Error	151.16	12			0.14	12		
Cor Total	60 110.57	24			2.33	24		

Note: * represents factor with a highly significant influence on the index ($0.01<p\leq 0.05$); ** represents factor with a significant influence on the index ($p\leq 0.01$).

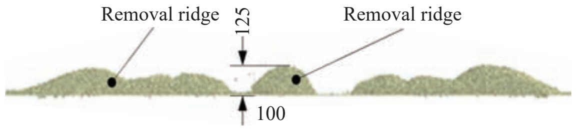

Figure 18 Simulation results of combined flexible brush, scraper, and rotary blade with optimal parameters

Table 16 Soil clearance index measurement results

	Ridge mass/kg										
	1	2	3	4	5	Average	Standard deviation (kg)	Coefficient of variation/ (*%)	Stability coefficient (%)	Soil removal rate (%)	Simulated soil removal rate ((%)
Primitive	429.3	455.15	397.85	464.25	438.1	436.93					
Ⅰ	121.7	136.45	119.85	117.25	129.65	124.98	7.91	6.33	93.67	71.40	69.68
Ⅱ	47.55	56.75	50.15	44.45	53.85	49.55	4.89	9.68	90.32	88.65	88.7

Note: Ⅰ: the scraping-rotating soil cleaning machine. Ⅱ: the scraping-rotating-brushing dehilling machine.

providing a technical foundation for the mechanization and intelligent evolution of grape orchards.

Acknowledgements

The authors acknowledge that this research was financially supported by Key R&D Project of Ningxia Hui Autonomous Region (Grant No. 2022BBF02042) and Ningxia Natural Science Foundation (Grant No. 2022AAC03258).

[References]

[1] Wang R, Sun Q, Chang Q R. Soil types effect on grape and wine composition in Helan Mountain area of Ningxia. PloS one, 2015; 10(2): e0116690.

[2] Jiang T T, Yan P K, Ma T H, Wang R. Nutritional requirements and precise fertilization of wine grapes in the eastern foothills of Helan Mountain. Int J Agric & Biol Eng, 2022; 15(4): 147–153.

[3] Davenport J R, Keller M, Mills L J. How cold can you go? Frost and winter protection for grape. HortScience, 2008; 43(7): 1966–1969.

[4] Poling E B. Spring cold injury to winegrapes and protection strategies and methods. HortScience, 2008; 43(6): 1652–1662.

[5] Van Leeuwen C. Terroir: the effect of the physical environment on vine growth, grape ripening, and wine sensory attributes. Managing Wine Quality, 2010; 83(2): 273–315.

[6] Li Y, Bardaji de Azcarate I. A new wine superpower? An analysis of the Chinese wine industry. Cahiers Agricultures 2017; 26(6): 1–8.

[7] Gilbert J A, van der Lelie D, Zarraonaindia I. Microbial terroir for wine grapes. Proceedings of the National Academy of Sciences, 2014; 111(1): 5–6.

[8] Niu C, Xu L M, Duan Z Z, Liu X X, Ma S, Yuan Q C, et al. Development of trellis-type grape winter buried soil clearing and cold-proof cloth recycling machine. Transactions of the CSAE, 2020; 36(2): 50–58.

[9] Yang Q, He M, Du G, Shi L, Zhao X, Shi A, et al. Design and experimental study of a wine grape covering soil-cleaning machine with wind blowing. AgriEngineering, 2021; 3(1): 50–72.

[10] Yang Q Z, Yang X Y, He M S, Zhang R Y, Wen T N, Shi A P. Design and experiment of the rotary throwing knife of wine grape cleaning machine. Transactions of the CSAE, 2022; 38(24): 44–51. (in Chinese)

[11] Ma S, Niu C, Yan C, Tan H, Xu L. Discrete element method optimisation of a scraper to remove soil from ridges formed to cold-proof grapevines. Biosystems Engineering, 2021; 210: 156–170.

[12] Dinu D G, Ricciardi V, Demarco C, Zingarofalo G, De Lorenzis G, Buccolieri R, et al. Climate change impacts on plant phenology: Grapevine (Vitis vinifera) bud break in wintertime in Southern Italy. Foods, 2021; 10(11): 2769.

[13] Droulia F, Charalampopoulos I. Future climate change impacts on European viticulture: A review on recent scientific advances. Atmosphere, 2021; 12(4): 495.

[14] Poni S, Sabbatini P, Palliotti A. Facing spring frost damage in grapevine: recent developments and the role of delayed winter pruning–a review. American Journal of Enology and Viticulture, 2022; 73(4): 211–226.

[15] Rahemi A, Fisher H, Carter K, Taghavi T. Mitigating grapevine winter damage in cold climate areas. Horticultural Science 2022; 49(2): 59–70.

[16] Zhang J X, Li J M, Wang Y C, Wang M B, Zhang P, Dong Z S, et al. Design, analysis and test of cleaning machine for grapevine cold-proof soil. Inmateh-Agricultural Engineering, 2022; 66(1): 229–238.

[17] Yang S M, She H Y, Yang S C, Zhu X J, Chen Y, Li J H, et al. Design and experimental validation of improved grapevine burying machine. Int J Agric & Biol Eng, 2018; 11(2): 95–100.

[18] Ma S, Xu L M, Xing J J, Yuan Q C, Yu C C, Duan Z Z, et al. Development of unilateral cleaning machine for grapevine buried by soil with rotary impeller. Transactions of the CSAE, 2018; 34(23): 1–10. (in Chinese)

[19] Xiong P Y, Yang Z, Sun Z Q, Zhang Q Q, Huang Y Q, Zhang Z W. Simulation analysis and experiment for three-axis working resistances of rotary blade based on discrete element method. Transactions of the CSAE, 2018; 34(18): 113–121.

[20] Kim Y-S, Siddique M A A, Kim W-S, Kim Y-J, Lee S-D, Lee D-K, et al. DEM simulation for draft force prediction of moldboard plow according to the tillage depth in cohesive soil. Computers and Electronics in Agriculture, 2021; 189: 106368.

[21] Zhao H B, Huang Y X, Liu Z D, Liu W Z, Zheng Z Q. Applications of discrete element method in the research of agricultural machinery: A review. Agriculture, 2021; 11(5): 425.

[22] Li B, Chen Y, Chen J. Modeling of soil–claw interaction using the discrete element method (DEM). Soil and Tillage Research, 2016; 158: 177–185.

[23] Ma S, Xu L M, Yuan Q C, Niu C, Zeng J, Chen C, et al. Calibration of discrete element simulation parameters of grapevine antifreezing soil and its interaction with soil-cleaning components. Transactions of the CSAE, 2020; 36(1): 40–49. (in Chinese)

[24] Zhang Z G, Xue H T, Wang Y C, Xie K T, Deng Y X. Design and experiment of panax notoginseng bionic excavating shovel based on EDEM. Transactions of the CSAM, 2022; 53(5): 100–111. (in Chinese)

[25] Liao Q X, Xu H M, Qingsong Z, Jiqin Z, Qian, A, Lei W. Design and experiment of driven disc plow and double-edged rotary tillage combined tiller. Transactions of the CSAM, 2023; 54(7): 99–110. (in Chinese)

[26] Ahmad F, Qiu B J, Ding Q S, Ding W M, Khan Z M, Shoaib M, et al. Discrete element method simulation of disc type furrow openers in paddy soil. Int J Agric & Biol Eng, 2020; 13(4): 103–110.

[27] Katinas E, Chotěborský R, Linda M, Jankauskas V. Wear modelling of soil ripper tine in sand and sandy clay by discrete element method. Biosystems Engineering, 2019; 188: 305–319.

[28] Zhang L, Zhai Y, Chen J, Zhang Z, Huang S. Optimization design and performance study of a subsoiler underlying the tea garden subsoiling mechanism based on bionics and EDEM. Soil and Tillage Research, 2022; 220: 105375.

[29] Kim Y-S, Lee S-D, Baek S-M, Baek S-Y, Jeon H-H, Lee J-H, et al. Development of DEM-MBD coupling model for draft force prediction of agricultural tractor with plowing depth. Computers and Electronics in Agriculture, 2022; 202: 107405.

[30] Saunders C, Ucgul M, Godwin R J. Discrete element method (DEM) simulation to improve performance of a mouldboard skimmer. Soil and Tillage Research, 2021; 205: 104764.

[31] Makange N R, Ji C, Torotwa I. Prediction of cutting forces and soil behavior with discrete element simulation. Computers and Electronics in Agriculture, 2020; 179: 105848.

[32] Wang X, Zhang S, Pan H, Zheng Z, Huang Y, Zhu R. Effect of soil particle size on soil-subsoiler interactions using the discrete element method simulations. Biosystems Engineering, 2019; 182: 138–150.

[33] Ucgul M, Fielke J M, Saunders C. Three-dimensional discrete element modelling (DEM) of tillage: Accounting for soil cohesion and adhesion. Biosystems Engineering, 2015; 129: 298–306.

[34] Sun J, Chen H, Wang Z, Ou Z, Yang Z, Liu Z, et al. Study on plowing performance of EDEM low-resistance animal bionic device based on red soil. Soil and Tillage Research, 2020; 196: 104336.

[35] Yan D, Yu J, Wang Y, Zhou L, Sun K, Tian Y. A review of the application of discrete element method in agricultural engineering: A case study of soybean. Processes, 2022; 10(7): 1305.

[36] Du J, Heng Y, Zheng K, Luo C, Zhu Y, Zhang J, et al. Investigation of the burial and mixing performance of a rotary tiller using discrete element method. Soil and Tillage Research, 2022; 220: 105349.

[37] Mudarisov S, Farkhutdinov I, Khamaletdinov R, Khasanov E, Mukhametdinov A. Evaluation of the significance of the contact model particle parameters in the modelling of wet soils by the discrete element method. Soil and Tillage Research, 2022; 215: 105228.

[38] Mudarisov S G, Gabitov I I, Lobachevsky Y P, Mazitov N K, Rakhimov R S, Khamaletdinov R R, et al. Modeling the technological process of tillage. Soil and Tillage Research, 2019; 190: 70–77.

[39] Zhou L, Lan Y B, Yu J Q, Wang Y, Yan D X, Sun K, et al. Validation and calibration of soil parameters based on EEPA contact model. Computational Particle Mechanics, 2023; 10: 1295–1307.

[40] Gomez K A, Gomez A A. Statistical procedures for agricultural research. John Wiley & Sons, 1984. doi: 10.2307/2530400

[41] Wan L P C, Li Y L, Zhang C, Ma X, Song J N, Dong X Q, et al. Performance evaluation of liquorice harvester with novel oscillating shovel-rod components using the discrete element method. Agriculture, 2022; 12(12): 2015.

[42] Petersen R G. Agricultural field experiments: design and analysis. CRC Press, 1994.